

THE SPECTRAL DISTRIBUTION
OF X-RAYS SCATTERED WITHIN A
WATER PHANTOM

A Thesis

Submitted to the Faculty of Graduate Studies
in Partial Fulfilment of the Requirements
for the Degree of
Master of Science
in the Department of Physics
University of Saskatchewan

by

Thomas J. Griffith

Written under the Supervision of
Drs. H.E. Johns and D.V. Cormack

Saskatoon, Saskatchewan

April, 1956

135595



OCT 18 '56

401000682689

ACKNOWLEDGEMENTS

The author is pleased to acknowledge the advice and assistance of Dr. D.V. Cormack and Dr. H.E. Johns. Thanks are also due Mr. Charles Kresse for his cooperation in instrumentation. Financial support for the project was supplied by the National Cancer Institute of Canada and the Saskatchewan Division of the Canadian Cancer Society. The use of the facilities of the Saskatoon Cancer Clinic is gratefully acknowledged.

Table of Contents

	<u>Page</u>
Introduction	1
The Apparatus	2
Data and Data Processing	8
(i) The Spectral Distribution of the Scattered Radiation.	8
(ii) The Relative Amounts of Forward and Back Scatter	10
(iii) The Total Radiation Spectra	10
Discussion of Trends in the Radiation Spectra	16
(i) Discussion of Potential Sources of Error	17
Applications of the Spectral Distribution of Radiation at Points Within a Phantom	19
(i) Calculation of Differential Absorption in Bone and Soft Tissue	19
(ii) Calculation of Half Value Layer for the Radiation at Central Axis Points Within the Phantom	22
(iii) Calculation of Linear Energy Transfer	25
Summary	27
Bibliography	
Appendix A: A Discussion of the Meaning of Linear Energy Transfer	29

List of Figures

	<u>Page</u>
Figure 1 The Experimental Apparatus	3
Figure 1a Schematic Representation of the Lucite Drum Assembly	3
Figure 2 The Photomultiplier and Impedance Matching Circuit	5
Figure 3 Sketch Showing the Relationship of the Collimator Dimensions to the Dimensions of the Lucite Pipe...	5
Figure 4 The Photon Spectra of Scattered Radiation at 45° , Depth 10 cm Produced by the Interaction of 400 KVP X-rays with Water	7
Figure 5 A Diagram to Aid in the Interpretation of the Steps Involved in Data Processing	7
Figure 6 The Angular Distribution of 100 KEV Radiation at Depth 10 cm Generated by 400 KVP X-rays in Water for Various Field Sizes	9
Figure 7 Photon Flux Distributions of Scattered Radiation Arising from 400 KVP X-rays at a Depth of 10 cm of Water	9
Figure 8 Photon Flux Distributions of Scattered Radiation at Various Depths Produced by 400 KVP X-rays, Field 400 cm^2 , F.S.D. = 62 cm.....	11
Figure 9 The Relative Contributions of Forward and Back Scattered Radiation to the Scattered Photon Spectra at Depths of 2 and 15 cm.....	11
Figure 10 The Relative Contributions of Primary and Scat- tered Radiation to the Total Dose Received at a Central Axis Point 10 cm Below the Surface of the Water when Irradiated with 400 KVP X-rays, HVL 3.8 mm of Copper.....	13
Figure 11 The Dose Received at Central Axis Points in a Water Phantom Irradiated with 400 KVP X-rays, HVL 3.8 mm of Copper.....	16

Figure 12 The Variation of Effective Wavelength with 23
 Depth of Scatterer
 (1) Clarkson and Mayneord, 1939, Primary
 HVL 4.4 mm of Copper.
 (2) Clarkson and Mayneord, 1939, Primary
 HVL 4.85 mm of Copper.
 (3) Cormack and Griffith, 1956, Primary
 HVL 3.8 mm of Copper.

List of Tables

Table	I	The Relative Spectral Distribution of the Scattered Radiation at Central Axis Points in the Phantom in Photons per cm ² per KEV Interval.....	14
Table	II	The Primary and Total Dose in Roentgens per KEV Interval at Central Axis Points in a Water Phantom Irradiated with 400 KVP X-rays, HVL 3.8 mm Copper.....	15
Table	III	Differential Absorption in Bone with Reference to Muscle.....	21
Table	IIIa	Differential Absorption in Fat with Reference to Muscle.....	21
Table	IV	The HVL of the Radiation Produced by the Interaction of 400 KVP, HVL 3.8 mm Cu, X-rays with a Water Phantom as Expressed in mm of Cu.....	24
Table	IVa	The Effective Wavelength of the Radiation Produced by the Interaction of 400 KVP, HVL 3.8 mm Cu X-rays with a Water Phantom as Expressed in Angstrom Units.....	24
Table	V	Mean Values of Linear Energy Transfer for Radiation at Points Within a Water Phantom Expressed in KEV per Micron.....	26

INTRODUCTION

The biological effects produced by an X-ray beam are dependent on the spectral distribution of the rays. Unfortunately a straightforward determination of this spectral distribution at a point within a biological medium is complicated by scattering processes which significantly alter the spectral distribution at the point from that of the primary radiation. Prior to the advent of the sodium iodide scintillation counter, direct measurements of the spectrum of the radiation inside a scattering medium were impossible although some information was obtained (1,2) using dual ionization chambers.

The application of a scintillation spectrometer to the measurement of the spectral distribution of scattered X-rays within a water phantom has, however, made it possible to obtain more detailed and more extensive information about the radiation. In particular, coupled with a prior investigation of the primary spectral distribution (3) the investigation of the scattered radiation here reported provides the total spectral distribution of the X-rays at central axis points within a phantom, the manner in which the biological effectiveness of the rays as expressed by linear energy transfer changes with depth and field size, and the differential absorption of the rays in bone and soft tissue for 400 KVP X-rays, HVL 3.8 mm of Cu.

THE APPARATUS

In Figures 1 and 1a is shown the experimental apparatus used in measuring the spectral distributions of the scattered X-rays. Essentially it consists of a cylindrical tank of sixteenth inch lucite, radius 22.5 cm, axial length 30 cm, with ends of one-half inch thick lucite, which can be rotated about its axis. A flat strip of sixteenth inch lucite is anchored along the axis of the tank to rigidly position the closed end of a one-half inch inner diameter lucite pipe. The other end of this radially mounted pipe is left open and is brought out through a seal in the cylindrical wall of the tank. Provision for filling the cylinder with water is made by means of hose connectors which are mounted in the end plates.

The collimator, scintillation counter, and shielding are co-axial with the lucite pipe and they are suspended from the same axle as the tank so that the whole assembly can be rotated as a unit. The collimator consists of cylindrical pieces of tin with $3/32$ inch holes inserted in a brass container which may be positioned within the lead shield by means of six screws. The scintillation counter which fits into the lead shield directly behind the collimator consists of a two inches long by inch and three-quarters diameter sodium iodide crystal butted against a photomultiplier tube. A cathode follower impedance matching circuit is attached to the base of the photomultiplier. The pulse, high voltage, and power cables are brought out of the shield via a baffle which prevents stray radiation leaking in the back of the crystal. To facilitate the taking of background counts, provision is made for

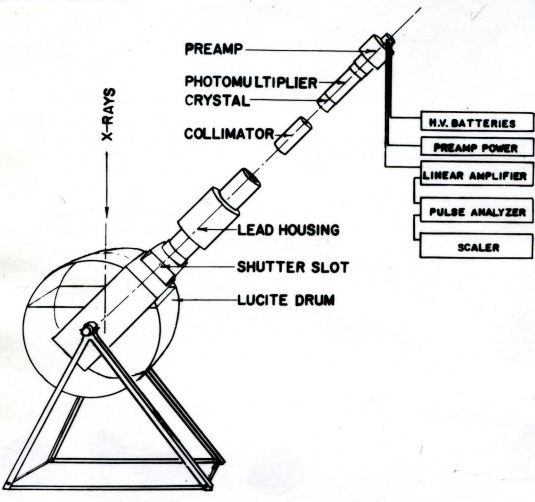


Figure 1 The Experimental Apparatus

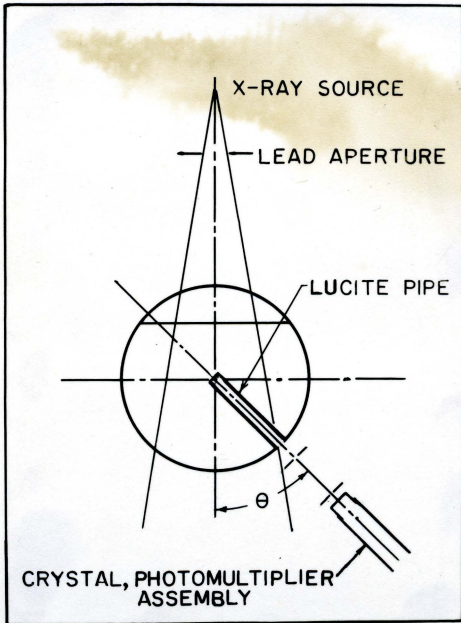


Figure 1a Schematic Representation of the Lucite Drum Assembly

the insertion of a one and three-quarter inch thick, lead shutter between the collimator and the tank. In counting the scattered radiation the shutter is replaced by a lead baffle which prevents radiation from leaking in around the collimator. The crystal and photomultiplier are wrapped with Scotch Electrical Tape to prevent stray light from entering the counter. To facilitate the energy calibration of the counter, there is a plug in the lead shield which may be removed to permit insertion of a vial of radio-iodine. The remaining components of the spectrometer are an Atomic 204B linear amplifier, an Atomic 510 single channel pulse height analyzer, a Marconi scaler, and a high voltage battery pack. A schematic diagram of the wiring other than that obtained commercially is shown in Figure 2.

In practice, X-rays from a 400 KV General Electric Maximar are directed vertically downward through apertures defined by heavy lead rings of diameter such as to give fields of 50, 100, 200, and 400 square centimeters at a focal skin distance of 62 centimeters. The interaction of this beam with water in the tank gives rise to scattered photons. Some of these photons have direction such that they pass through the end of the lucite pipe and of these, some have direction (Figure 3) such that they pass through the collimator to the crystal.

The routine procedure for taking data was as follows:
The defining lead ring was selected to give the desired field size. The tank was filled with water to the desired depth and the F.S.D. adjusted to 62 centimeters. The assembly was then set at the angle θ at which the spectrum was to be obtained, the lead shutter inserted,

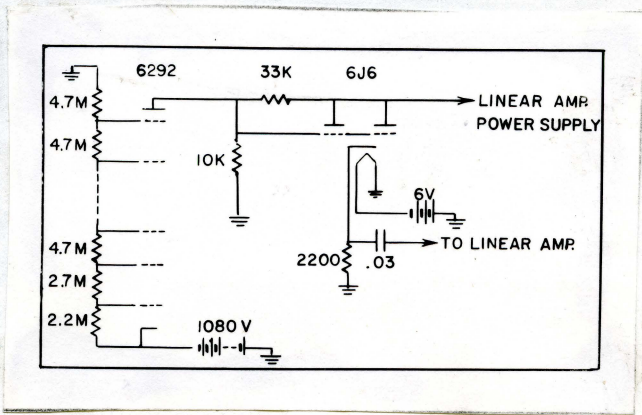


Figure 2 The photomultiplier and Impedance Matching Circuit.

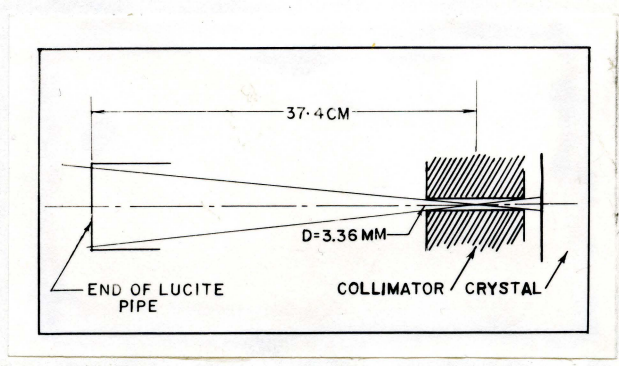


Figure 3 Sketch showing the relationship of the collimator dimensions to the dimensions of the lucite pipe and how the photons admitted to the crystal are limited to those which pass through the end of the lucite pipe.

the X-rays turned on, and a background count taken for each setting of the baseline control on the pulse height analyzer. With the X-rays off, an energy calibration of the base line scale was made by inserting a small vial of radioactive iodine in the calibration hole in the shield and then finding those settings of the baseline control on the analyzer which corresponded to the center of the 364KV and 80KV photopeaks arising from the iodine. The plug was then replaced in the shield, the shutter removed and replaced with the baffle, the X-rays turned on, and the spectrum of the radiation determined. Throughout the experiment the channel width control of the analyzer was kept at two volts. Linearity of the baseline control had been established previously (3). Additional energy calibrations were made as required. Spectra were obtained for all four areas at angles of 15, 30, 45, 60, 75, 90, 105, and 135 degrees and for depths of 0, 2, 4, 6, 10, and 15 centimeters of water above the lucite pipe.

Some typical spectra are shown in Figure 4. The data shown are as taken with the exception of the conversion from baseline settings to K.E.V.

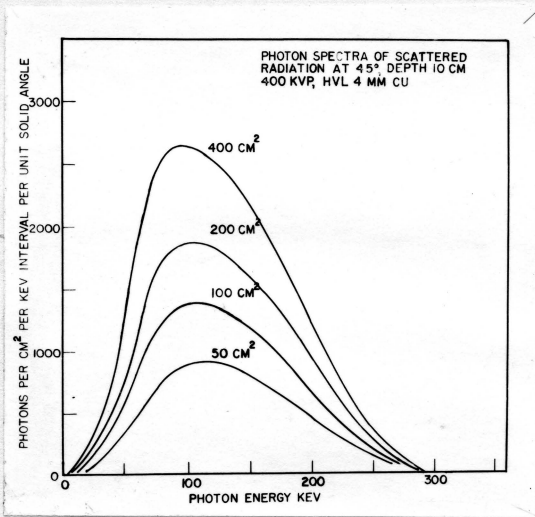


Figure 4 The Photon Spectra of Scattered Radiation at 45°, Depth 10 cm Produced by the Interaction of 400 KVP X-rays with Water.

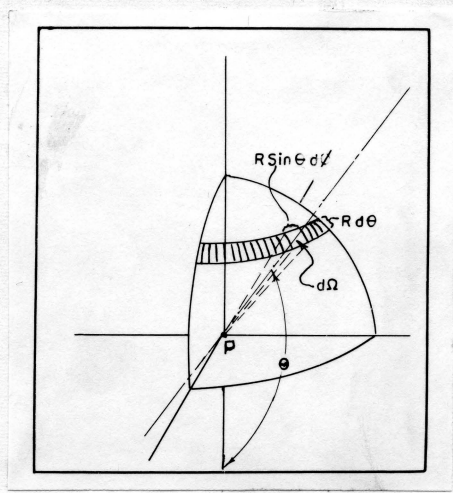


Figure 5 An Illustration of the Steps Involved in Processing the Experimental Data to Obtain the Complete Spectral Distribution of Scattered X-rays at a Point within a Phantom.

DATA AND DATA PROCESSING

The Spectral Distribution of the Scattered Radiation

The spectra obtained by the routine outlined above can be interpreted in terms of Figure 5. In Figure 5 the point P represents a point on the central axis of the X-ray beam at the end of the lucite pipe. The solid angle $d\Omega$ is the angle which P subtends at the surface of the crystal. Spectra of the type illustrated in Figure 4 give the number of photons passing through P with paths included in $d\Omega$ with any particular energy k . We shall refer to these spectra as $\phi(k, \theta)$ vs. k . Because radial symmetry exists with respect to the axis of the primary X-ray beam, we may integrate $\phi(k, \theta)$ over an azimuthal angle simply by multiplying by $2\pi \sin \theta$; that is, we can obtain the spectral distribution of photons which pass through P and a band on the surface of a sphere such as is shown in part by the shaded area of Figure 5*.

At this stage we have the spectral distribution of photons passing through P from any angle θ . The distribution at P of scattered photons from all angles is obtained by integrating $2\pi\phi(k, \theta) \sin \theta$ over θ . This is done by taking the values of this function at each angle of measurement θ for a particular field, depth, and value of k and plotting these values against θ . An example of such a plot is shown in Figure 6. The areas under these curves are then measured with a planimeter to obtain

$2\pi \int_0^{\pi} \phi(k, \theta) \sin \theta d\theta$. Repeating the integration for different

values of k and then plotting the values of the integrals against k

*The radial factor was omitted from the integration; the ordinates of the spectra obtained are proportional to the actual numbers of photons/cm²/KEV interval.

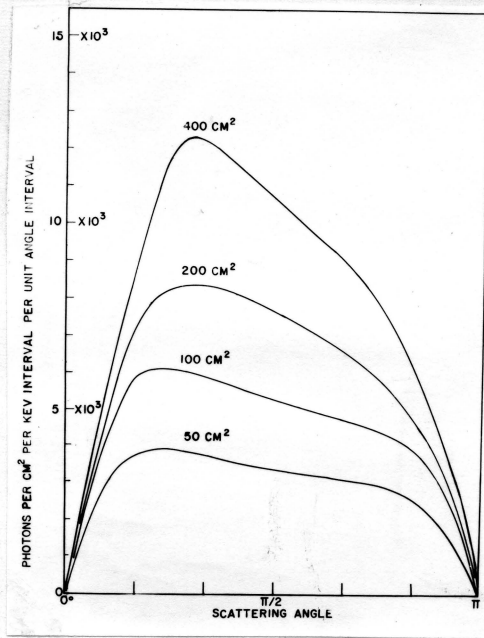


Figure 6 The Angular Distribution of 100 KEV Radiation at Depth 10 cm Generated by 400 KVP X-rays in Water for Various Field Sizes.

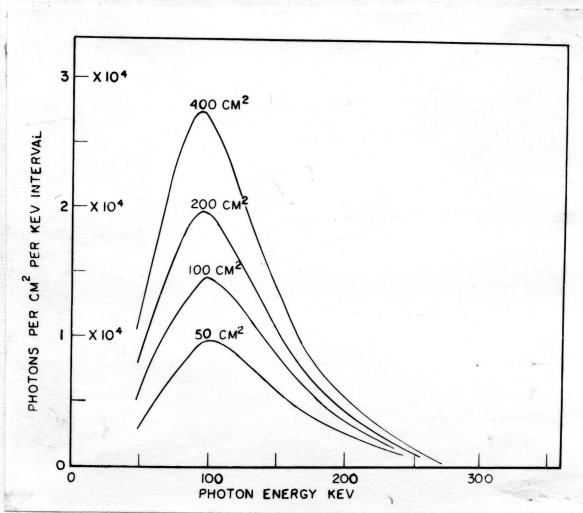


Figure 7 Photon Flux Distributions of Scattered Radiation Arising from 400 KVP X-rays at a Depth of 10 cm of Water.

yields the spectral distribution of the scattered radiation at P. Examples of these spectra of scattered radiation are shown in Figures 7 and 8. In Table 1 are given the values of $2\pi \int_0^\pi \phi(k, \theta) \sin\theta \, d\theta$, the number of photons per square centimeter per KEV interval for the various values of k.

The Relative Amounts of Forward and Back Scattered Radiation

In the integration over the angle θ described in the previous section, the area may be measured in two parts, one from zero to $\frac{\pi}{2}$ and the other from $\frac{\pi}{2}$ to π . These components of the area represent the forward scattered photons and the backward scattered photons respectively. A graph showing their relative magnitudes and the effect of depth of scattering material on the relative magnitudes is presented in Figure 9 for the 400 square centimeter field.

The Total Radiation Spectrum

To obtain the total radiation spectrum at a point within the phantom, the primary spectrum must be added to the scattered spectra determined above. To do this it was necessary to adjust all data to some arbitrary surface dose using the depth dose tables (4) as a basis for normalization.

The first step in the process was to convert the scattered photon distributions to dose distributions. This was accomplished by multiplying the values of $2\pi \int_0^\pi \phi(k, \theta) \sin\theta \, d\theta$ in Table 1 by the number of roentgens per photon of energy k, a factor which was obtained from White's tables (5). These numbers were then plotted

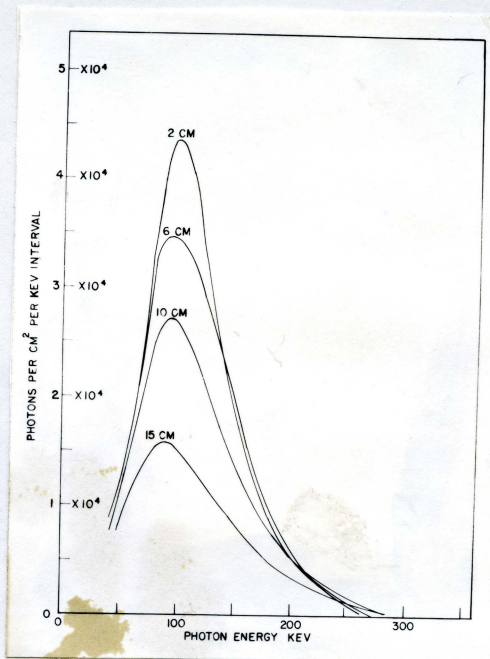


Figure 8 Photon Flux Distributions of Scattered Radiation at Various Depths produced by 400 KVP X-rays, Field = 400 cm^2 , F.S.D. = 62 cm.

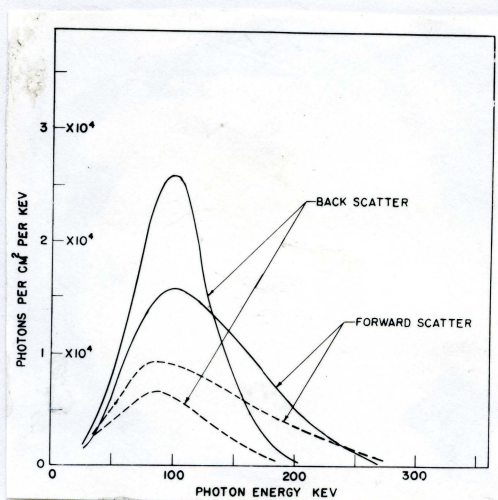


Figure 9 The Relative Contributions of Forward and Back Scattered Radiation to the Scattered Photon Spectra at Depths of 2 and 15 cm.

----- 2 cm curves
 - - - - 15 cm curves

against energy to give the scattered dose spectra. The areas under these curves were measured using a planimeter.

The dose spectrum of the primary beam (3) was then plotted to an arbitrary scale. An area was chosen on the basis of this scale such that if this area were used as a basis for normalization, all spectra could be conveniently plotted to the same scale. The area expressed in planimeter units was taken to represent 10^4 roentgens. The ordinates of the primary spectrum were then multiplied by the ratio of the area under the arbitrarily plotted curve to the area chosen to represent 10^4 roentgens. Replotting these modified ordinates gave a primary dose distribution enclosing an area representing 10^4 roentgens.

The dose due to scattered radiation at 0, 2, 4, 6, 10, and 15 centimeter depths in the phantom for fields of 50, 100, 200, and 400 square centimeters from radiation of HVL 4mm Cu, FSD = 60cm was computed from the depth dose tables by multiplying 10^4 roentgens by the backscatter factor for the field under consideration and by the percentage depth dose for the depth under consideration and then subtracting the zero area depth dose ^{$\times 10^4 r$} from the product. The areas under the scattered distributions were normalized to these computed areas.

The dose at depths of 2, 4, 6, 10, and 15 centimeters due to primary photons of various energies was computed using $I = I_0 e^{-\mu d}$ where I represents dose from photons of energy k , I_0 the contribution to the $10^4 r$ surface dose from photons of this energy, μ the total absorption coefficient for photons of this energy, and d the depth in the phantom. Integration over all energies was performed to obtain the total primary dose for each depth and area.

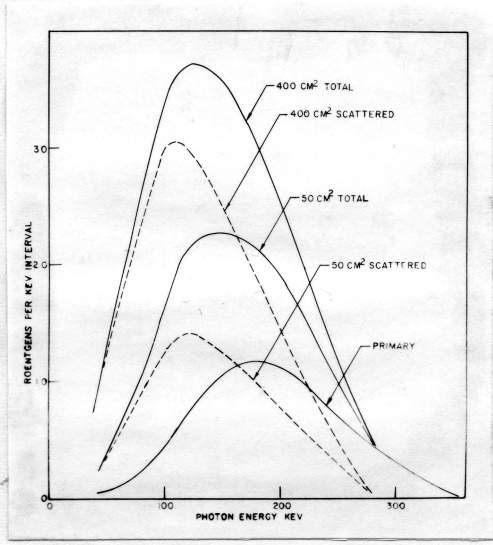


Figure 10 - The Relative Contributions of Primary and Scattered Radiation to the Total Dose Received at a Central Axis Point 10 cm. Below the Surface of the Water when Irradiated with 400 KVP X-rays, HVL 3.8 mm Cu.

The data used in plotting the total dose spectra are given in Table 11. A graph showing the relative contribution of primary and scattered radiation to the total dose is shown in Figure 10. The variation in the total dose spectrum with change in depth is shown in Figure 11.

Table I The Relative Spectral Distribution of the Scattered Radiation at Central Axis Points in the Phantom in Photons/cm²/KEV Interval. (The Values Given in the Table are Values of $\pi \int_0^\pi \phi(k, \theta) \sin \theta d\theta$)

Depth cm	Area cm ²	Energy - KEV									
		40	60	80	100	120	140	160	180	200	240
0	400 ^a	56	144	312	442	303	152	67	16		
2	50	23	-	112	158	144	-	73	-	32	10
	100	38	-	176	234	208	-	97	-	40	12
	200	54	-	226	288	262	-	124	-	46	14
	400	76	-	322	387	313	-	138	-	52	16
4	50	27	59	119	158	145	115	80	63	36	14
	100	41	95	177	220	203	156	106	74	47	19
	200	56	130	274	300	267	203	134	88	54	21
	400	82	191	320	366	326	244	153	98	61	25
6	50	25	62	91	114	109	85	63	47	30	13
	100	42	87	150	182	163	123	91	63	42	16
	200	60	134	218	245	221	166	114	67	53	19
	400	86	187	288	313	280	211	141	95	64	22
10	50	21	46	72	86	80	63	45	33	23	9
	100	39	80	119	131	115	89	65	45	31	12
	200	62	113	165	176	151	112	84	58	39	15
	400	80	162	233	239	203	148	107	71	48	20
15	50	15	25	43	47	42	34	25	16	14	6
	100	24	54	69	71	61	51	37	26	19	8
	200	40	78	103	103	85	67	50	35	25	12
	400	58	108	143	139	113	91	66	45	30	13

^a Since no change in the shape of the backscatter spectrum with change in field was observed, the best set of data, which is presented here, was used for normalization.)

Table II The Primary and Total Dose in Roentgens per KEV Interval at Central Axis Points in a Water Phantom Irradiated with 400 KVP X-rays, HVL 3.8 mm Cu. 15

Depth cm	Area cm ²	Energy - KEV														
		40	60	80	100	120	140	160	180	200	220	240	260	280	300	320
0	0	4.5	8.2	16.1	30.9	45.9	58.0	64.6	63.4	58.8	50.1	39.2	29.0	20.0	13.1	7.6
	50	7.3	13.1	27.6	51.2	62.8	68.2	69.8	64.8							
	100	8.1	14.8	31.6	58.1	69.2	72.1	71.8	65.3							
	200	8.8	16.1	34.6	63.4	73.0	74.3	73.0	65.7							
	400	9.5	17.5	37.7	68.9	77.5	77.1	74.4	66.1	Y	Y	Y	Y	Y	Y	Y
2	0	2.7	4.8	10.5	20.0	31.4	41.4	45.1	44.8	42.1	36.3	28.5	20.6	14.7	9.7	5.8
	50	6.8	13.0	25.3	45.9	60.3	66.5	65.8	62.0	54.3	44.5	33.3	20.6			
	100	8.4	16.0	30.8	53.3	67.3	71.0	68.8	64.5	55.3	45.0	33.4	21.0			
	200	9.8	17.0	33.4	56.1	71.3	75.0	72.0	65.5	56.5	45.5	33.5	21.5			
	400	13.5	23.8	41.0	62.8	73.9	77.4	74.1	67.8	59.1	48.1	35.5	22.0	Y	Y	Y
4	0	1.5	3.0	6.8	13.4	21.4	27.6	31.4	31.8	30.1	26.2	20.7	15.1	10.9	7.2	4.3
	50	6.1	9.7	21.9	37.9	48.7	53.9	53.2	50.0	43.1	34.5	27.0	18.0			
	100	7.5	12.7	26.6	43.7	55.4	59.0	56.8	52.4	45.1	37.5	28.2	18.2			
	200	8.7	14.7	33.7	49.8	60.7	63.6	59.6	53.4	45.3	38.0	29.0	18.4	Y	Y	Y
	400	12.4	22.9	39.0	59.0	70.7	72.1	64.5	56.4	47.8	38.5	29.7	18.6			
6	0	0.8	1.9	4.5	9.0	14.7	19.1	22.2	22.6	21.7	19.0	15.1	11.1	8.0	5.3	3.2
	50	5.5	9.8	17.5	29.1	38.0	40.8	41.1	39.2	33.9	28.0	21.8	13.5			
	100	7.3	11.4	22.3	35.7	43.7	45.5	45.3	41.3	36.0	30.0	21.9	13.7			
	200	9.5	15.6	28.8	42.8	51.6	52.5	49.4	41.3	38.6	31.0	22.6	13.9			
	400	12.9	20.2	35.2	50.0	59.2	59.5	54.0	47.7	41.2	32.5	23.3	14.1	Y	Y	Y
10	0	0.3	0.8	1.9	4.1	7.4	9.3	11.0	11.4	11.2	9.9	8.1	5.9	4.4	3.0	1.8
	50	3.6	5.7	10.4	16.5	21.5	22.4	22.5	21.2	19.1	16.3	12.0	8.2			
	100	6.1	9.2	15.4	22.6	27.1	27.6	26.9	24.2	21.5	17.8	13.2	8.6			
	200	9.0	11.8	19.4	27.2	31.4	30.9	29.9	26.8	23.0	18.4	13.8	9.0			
	400	10.8	17.6	25.9	34.1	37.4	36.3	34.0	29.9	25.7	19.6	14.6	9.2	Y	Y	Y
15	0	0.1	0.2	0.7	1.5	2.7	3.8	4.6	5.0	5.0	4.5	3.7	2.8	2.1	1.4	0.9
	50	2.2	2.6	5.6	8.1	9.7	10.5	10.4	9.3	9.3	7.8	6.3	4.1			
	100	3.7	6.0	8.7	11.7	13.4	14.5	13.7	12.7	11.3	9.4	7.2	4.6			
	200	5.7	7.7	11.6	15.1	16.2	16.7	16.0	14.4	12.4	10.4	8.0	5.0			
	400	7.9	10.7	15.8	19.2	20.7	20.9	19.4	16.8	14.0	11.5	8.6	5.4	Y	Y	Y

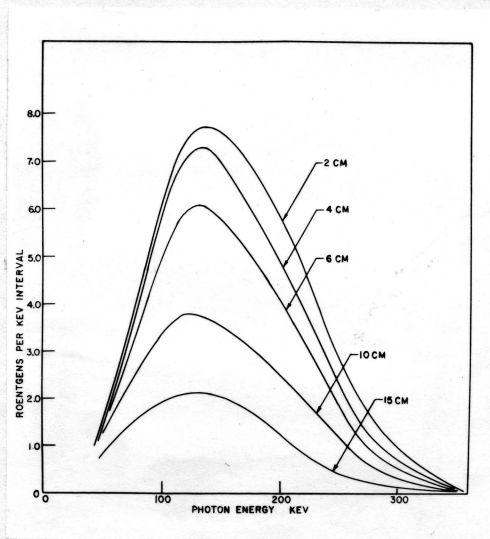


Figure 11 The Dose Received at Central Axis Points in a Water Phantom Irradiated with 400 KVP X-rays, HVL 3.8 mm Cu. (Data based on 10^{14} r primary surface dose)

DISCUSSION OF TRENDS IN THE RADIATION SPECTRA

Perhaps the most significant feature of the spectra is the absence of any marked change in shape for changes in area or in depth. This implies that any change in biological effectiveness is slight as is shown in the section of the thesis which deals with applications.

In Figure 11 is shown the total radiation at depths from two to 15 centimeters. The effect of increasing depth in this range appears to be a shift of the spectrum to lower energies. This trend is further confirmed by the calculation of HVL and differential absorption in the section on applications. The curve for 15 cm in Figure 11 does not show the trend to lower energies so much by the location of its maximum as by the attenuation of the high energy component. This trend to lower energies is the result of attenuation of the primary but is moderated by the effective filtration of the primary.

With respect to area the spectra clearly show the shift to lower energy with increasing field size. As is shown in Figure 10 this is attributable to the relatively large contributions of the scattered radiation to the total dose with large fields as contrasted to small fields. The scattered photon spectra, as shown in Figures 7 and 8, exhibit the same trend as the total spectra. Figure 9, showing the relative amount of forward to back scatter, shows the effect of filtration of the primary as revealed by the smaller percentage decrease in the forward scatter with increased depth than in back scatter. This indicates that there is a greater proportion of high energy photons in the primary at 15 cm than at 2 cm.

A Discussion of Potential Sources of Error

Examination of the experimental apparatus raises the following questions: To what extent is the volume of water giving rise to scattered photons changed by the lucite pipe? Is the lucite itself likely to alter the spectra obtained? Is there significant absorption of soft energy radiation in the air between tube and counter?

A quick calculation of absorption of low energy photons in air rules out this as a source of error. Lucite is a more effective scatterer than water, but the difference is probably slight. Further, since what is really desired is the scatter within tissue or tissue equivalent material, the spectra obtained in the presence of lucite are probably as good an approximation to the desired spectra as they would be without lucite. The effect on the spectrum of radiation at a point produced by replacing some of the scattering material around the point by a volume of air is negligible, for the following reasons:

The photon contribution which water in the pipe volume would make to the spectrum at a point at the end of the pipe as measured must arise from photons which have undergone at least two scatterings. The probability that the second scattering will give rise to a photon with path in the solid angle subtended by the collimator is small. The volume of the tube is not large compared to the total volume which gives rise to scattered photons.

The sharp fall off of low energy radiation (Figure 4) was viewed with suspicion. Having ruled out air absorption, the packing of the sodium iodide crystal was investigated. The outer coating of 0.082 cm Al and reflective coating of 0.238 cm of MgO could produce as much as a 10 per cent decrease in radiation of 30 KV or less. However, when the measurement was made with a sodium iodide crystal which had only a thin aluminium surface, no increase in the proportion of low energy photons was observed.

The linear energy response of this crystal to radiation in the energy range used has been discussed elsewhere (3). Corrections for the Gaussian spread of pulses were made for the photon spectra shown in Figures 7 and 8. However, the corrections for K escape photons (6) and Gaussian spread as revealed by preliminary calculations (7) are very small and would be greatest at low energies where the spectral intensity is already low and the statistical accuracy of the data limited. Therefore, the data presented in Tables I and II as well as the subsequent calculations based on these data are not corrected for these effects.

APPLICATIONS OF THE SPECTRAL DISTRIBUTION OF RADIATION AT POINTS WITHIN
A PHANTOM

Calculation of Differential Absorption in Bone and Soft Tissue

Given the spectral distribution of the scattered radiation and the absorption coefficients for bone, fat, and muscle, the differential absorption of the radiation may be calculated. The energy delivered by the X-rays to a point in the phantom is expressed by $\int_0^{k_{\max}} N(k) \cdot k(\mu_a/\rho) dk$ where N is the number of photons per square centimeter per KEV interval with energy k and μ_a/ρ is the real mass absorption coefficient of the material for photons of energy k . The quantity, $N(k) k$ is equal to the number of roentgens times the energy per ion pair in air divided by the real mass absorption coefficient of air.

$$N(k) \cdot k = [D(k) \cdot W] / (\mu_a/\rho)_{\text{air}}$$

The energy absorbed in any material may be expressed as

$$\int_0^{k_{\max}} \{ [D(k) \cdot W \cdot (\mu_a/\rho)_{\text{material}}] / (\mu_a/\rho)_{\text{air}} \} dk$$

and the differential absorption between two materials by the ratio of two such integrals. In particular, for the differential absorption of bone to soft tissue the expression is

$$\frac{W \int_0^{K_{\max}} \{ [D(k) \cdot (\mu_a/\rho)_{\text{bone}}] / (\mu_a/\rho)_{\text{air}} \} dk}{W \int_0^{K_{\max}} \{ [D(k) \cdot (\mu_a/\rho)_{\text{muscle}}] / (\mu_a/\rho)_{\text{air}} \} dk}$$

To obtain and evaluate the ratio of these integrals, the ratios of the real mass absorption coefficients, $(\mu_a/\rho)_{\text{bone}} : (\mu_a/\rho)_{\text{air}}$, $(\mu_a/\rho)_{\text{fat}} : (\mu_a/\rho)_{\text{air}}$, $(\mu_a/\rho)_{\text{muscle}} : (\mu_a/\rho)_{\text{air}}$, were computed from the data of Spiers (8) and graphed as a function of energy k . The integrals



$\int_0^{k \text{ max}} [D(k) (\mu_a/P)_{\text{bone}} / (\mu_a/P)] dk$ were then evaluated by breaking them up into integrals over small intervals. That is, the products, (mid-interval dose x mid-interval absorption coefficient ratio x width of energy interval), were summed to give the total absorption.

The differential absorption for various areas and depths as given by the quotients of these integrals is tabulated in Table III. Of the changes in differential absorption revealed by the data of Table III, little significance is attached to the changes relating to fat and muscle. The changes in the differential absorption in bone however reveal increasing absorption in bone as the field size is increased. This is the result of the increase in scattered radiation with increased area and the consequent decrease in HVL. Since the photoelectric cross-section for calcium in the bone rises more rapidly with decreasing energy than that for water and the lower atomic number constituents of soft tissue, the differential absorption in bone rises. The data also shows that the change with area is more pronounced between zero and 50 square centimeters than between 50 and 400 square centimeters. The effect of filtration of the primary by increasing depths of water is very evident. The low value of differential absorption in bone for the primary at 15 centimeters as compared with the value for the 400 square centimeter field at that depth reveals a far more abrupt change with area than the corresponding data at the surface.

Table III Differential Absorption in Bone with Reference to Muscle

Depth cm	Area - Cm ²				
	0	50	100	200	400
0	1.27	1.36	1.39	1.41	1.43
2	1.24	1.36	1.42	1.44	1.50
4	1.22	1.38	1.43	1.46	1.56
6	1.21	1.37	1.47	1.52	1.58
10	1.18	1.43	1.53	1.60	1.68
15	1.14	1.44	1.57	1.61	1.74

Table III_a Differential Absorption in Fat with Reference to Muscle

Depth cm	Area - Cm ²				
	0	50	100	200	400
0	0.99	0.98	0.99	0.98	0.98
2	1.03	0.98	0.98	0.97	0.98
4	1.02	0.98	0.96	0.98	0.96
6	1.00	0.98	0.97	0.96	0.96
10	1.00	0.98	0.96	0.96	0.95
15	1.00	0.98	0.96	0.96	0.94

Calculation of Half Value Layer for the Radiation at Central Axis
Points Within the Phantom

Knowing the dose spectrum and the wavelength dependence of the total absorption coefficient of copper, it is possible to express the quality of the radiation within the phantom in terms of HVL and an "effective wavelength". The procedure follows from the definition of HVL,

$$0.5 = \frac{\int_0^{k_{\max}} D(k) e^{-\mu d} dk}{\int_0^{k_{\max}} D(k) dk}$$

in which d is the half value layer in centimeters of copper, $D(k)$ the dose in roentgens per KEV interval, and μ the linear absorption coefficient for copper expressed in reciprocal centimeters.

Rather than attempt a direct solution of this equation for d , the ratio of the two integrals was worked out for trial values of d . On the basis of preliminary calculations (9) it was decided that once two trial values of d yielded ratios straddling 0.5 had been obtained, then the actual HVL could be obtained without appreciable error, by simply plotting the two ratios versus d on a semi-log scale and interpolating for the value of d corresponding to a ratio of 0.5. The values of HVL so obtained are given in Table IV.

The actual process of evaluation of the ratio was one of cumulative multiplication of products of the form $D(k) e^{-\mu d} \Delta k$ where Δk is one of the energy intervals into which the range of energies, zero to k_{\max} , is divided.

For each value of HVL an effective wavelength was computed, this wavelength being the wavelength of monochromatic radiation having the same HVL of copper. These are given in Table IVa. Superficial

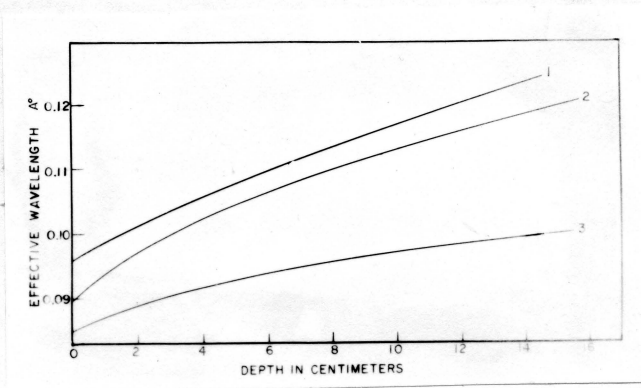


Figure 12 The Variation of Effective Wavelength with depth of scatterer

1. Clarkson and Mayneord, 1939, Primary HVL 4.4 mm Cu.
2. Clarkson and Mayneord, 1939, Primary HVL 4.85 mm Cu.
3. Cormack and Griffith, 1956, Primary HVL 3.8 mm Cu.

comparison of these data with the data of Clarkson and Mayneord (1) and Greening and Wilson (2) reveals a common increase in effective wavelength with depth of scatterer. The data of Clarkson and Mayneord (Figure 12) show a more rapid change in wavelength for small depths than was measured with the spectrometer. This is surprising in view of the heavy filtration of the primary employed by Clarkson and Mayneord. Comparison with the data of Greening and Wilson is difficult because of the very different primary HVL used. However, the initial hardening of the scattered component which they observed is also apparent in the data obtained by spectrometer. For the 50 cm² field the surface scattered radiation the spectrometer gives an effective wavelength of 0.12 Angstroms while for two centimeters depth the value is 0.10 Angstroms. For a field of approximately the same size, Greening

Table IV The HVL of the radiation produced by the interaction of 400 KVP, HVL 3.8 mm Cu., X-rays with a water phantom as expressed in mm of Cu.

Depth (cm)	Field Area (cm ²)				
	0	50	100	200	400
0	3.81	3.46	3.36	3.27	3.22
2	3.89	3.38	3.24	3.20	3.05
4	3.96	3.35	3.22	3.10	2.96
6	4.04	3.29	3.13	2.95	2.82
10	4.16	3.27	3.00	2.82	2.66
15	4.31	3.21	2.90	2.72	2.58

Table IVa The effective Wavelength of the radiation produced by the interaction of 400 KVP, HVL 3.8 mm Cu., X-rays with a water phantom as expressed in Å.

Depth (cm)	Field Area (cm ²)				
	0	50	100	200	400
0	0.075	0.081	0.082	0.084	0.085
2	0.074	0.082	0.084	0.085	0.088
4	0.073	0.083	0.085	0.087	0.090
6	0.072	0.084	0.086	0.090	0.093
10	0.070	0.084	0.088	0.093	0.097
15	0.068	0.085	0.091	0.095	0.099

and Wilson found a decrease of about 0.07 Angstroms in the effective wavelength of the scattered radiation.

Calculation of Linear Energy Transfer¹

A further use made of the total dose spectra was their application to the computation of an average linear energy transfer, L.E.T., which serves as a measure of the biological efficiency of the radiation. Using the data presented in Table II calculations were made to determine whether the efficiency of the radiation is appreciably altered by the scattering processes that occur in the water phantom. These calculations, the results of which are presented in Table V, revealed only a slight change in mean L.E.T. over the range of field areas and depths used in this experiment.

The procedure used for calculation of the L.E.T.'s recorded in Table V has been reported elsewhere (10). In outline, it consists of expressing the ordinates of the total dose spectra in photons per square centimeter per KEV interval, calculation of the initial distribution of electron energies, and the initial electron flux distributions produced by the radiation spectra (11). Then using values of L (9), the mean L.E.T. may be calculated from the formula

$$\bar{L} = \frac{\sum_0^{E \text{ max}} N(E) \cdot L(E) \Delta E}{\sum_0^{E \text{ max}} N(E) \cdot \Delta E}$$

where ΔE is one of the energy intervals comprising the total range of electron energy, $N(E)$ the value of electron flux at the middle of the interval, and $L(E)$ the mid-interval value of linear energy transfer for electrons of energy E .

¹ See appendix A for a brief discussion of the meaning of Linear Energy Transfer.

Table V Mean Values of Linear Energy Transfer for Radiation at Points Within a Water Phantom Expressed in KEV per micron.

Depth (cm)	Area (cm ²)				
	0	50	100	200	400
0	0.88	0.93	0.95	0.96	0.97
2	0.86	0.95	0.96	0.98	0.98
4	0.86	0.93	0.96	0.98	1.02
6	0.85	0.95	0.98	1.00	1.02
10	0.83	0.96	1.00	1.01	1.05
15	0.82	0.95	0.98	1.01	1.05

SUMMARY

The measurements of the spectral distribution of radiation generated by the interaction of 400 KVP X-ray with water show that the distribution is an insensitive function of field size and depth of scatterer. The same is true of the total radiation, primary plus scatter, at points on the central axis of the phantom. The measurements show that the radiation becomes less isotropic with depth, forward scatter predominating at greater depths. That a slight shift to lower energies with increasing area and depth does occur is shown by the decreased half value layer of the radiation at depth 15 cm, area 400 cm² as compared with the primary radiation. This shift produces an increasing differential absorption in bone with increasing depth and area of field. The biological effectiveness of the radiation expressed in L.E.T. is almost independent of field and depth.

Bibliography

1. Clarkson, J.R. and Mayneord, W.V.: Brit.J.Rad. 12, 168, 1939.
2. Greening, J.R. and Wilson, C.W.: Brit.J.Rad. 24, 605, 1951.
3. Cormack, D.V., Till, J.E., Whitmore, G.F., and Johns, H.E.: Brit.J.Rad. 28, 605, 1955
4. Central Axis Depth Dose Data: Brit.J.Rad. Supplement 5.
5. White, G.R.: National Bureau of Standards Report 1003, 1952.
6. Axel, P.: U.S.A.E.C. Report, B.N.L. 271, 1953.
7. Cormack, D.V.: Private Communication.
8. Spiers, F.W.: Brit.J.Rad. 19, 52, 1946.
9. Cormack, D.V.: Private Communication.
10. Cormack, D.V.: Indian J. Rad. In Publication 1956.
11. Johns, H.E., Till, J.E., and Cormack, D.V.: Nucleonics 12, 10, 40, 1954.

APPENDIX A: The Meaning of Linear Energy Transfer

Biological effects of X-rays are produced by the dissipation of photon energy in biological materials by a transfer of the photon energy to electrons via photoelectric effect, Compton effect, and, for energies greater than those used in this experiment, pair production. To express in detail the way in which the energy is eventually degraded from the initial kinetic energy of the electrons requires several questionable assumptions about ionizations and excitations in tissue. The concept of linear energy transfer explained below avoids these assumptions by dealing only with the energy lost by the electrons, not with the reactions in which it is lost.

If we consider the passage of an electron through a cloud chamber, we see a track composed of condensations about ions produced by the electron. The ion density varies over the length of the track, but for suitably short segments of track a value of energy transfer per unit length can be defined. If we are interested in the energy absorbed in a region about the track, this value must include information about secondary electrons or Δ -rays. That is, the total energy which the electron loses to the region would be obtained by determining the number of ionizations along the main track and also along secondary spurs and segment of spurs which lie within the region of interest.

Assuming similar events to occur in tissue as in air, although within a much more restricted space, we define an L.E.T. for radiation to describe the loss of energy by electrons set in motion by that radiation. As in gas, the rate of exchange of energy between the electrons and the medium they traverse depends upon the energy of the electrons or the segment of track considered. That is, the stopping power of the material for electrons is a function of electron energy. Were we to neglect the contribution of secondary electrons or γ -rays, our value of L.E.T. would be the collisional stopping power of the material for electrons. However, in order for our L.E.T. values to apply to calculations of energy locally absorbed, the energy carried away by the γ -rays must be considered. This is done by modifying the collisional stopping power which normally gives the total cross-section for collisional processes in which an electron loses up to half its kinetic energy. Instead we find the total cross-section for collisional processes in which the electron loses energy up to $E' < E/2$. E' determines the maximum range of secondary electrons giving up energy in the volume of interest and this range will define what is meant by 'locally absorbed'. Collisions in which electrons lose energies greater than E' will result in γ -rays which do not give up their energy locally. The L.E.T. values in Table V were determined using an $E' = 0.5$ KEV.

